International Forum on Aeroelasticity and Structural Dynamics
IFASD 2015
June 28 — July 02, 2015 ▲ Saint Petersburg, Russia

AN ADVANCED PANEL METHOD FOR COMPRESSIBLE SUBSONIC UNSTEADY FLOW PAST COMPLEX GEOMETRIES

Steven P. Fiddes, Chris W. Burkett[1] and Thiemo Kier [2]

[1]Flow Solutions Limited, Chipping Sodbury, UK

[2]Institute of System Dynamics and Control, German Aerospace Center (DLR), Weßling, Germany

Abstract: This paper describes the development of a new boundary-element method for predicting the unsteady compressible flow past general configurations in subsonic flow. It permits the actual geometry of the configuration to be represented and computes the coupling between the steady and unsteady flow components. It adopts a description of the unsteady deformation of the geometry that avoids many of the limitations inherent with vortex- and doublet-lattice methods. The paper describes the issues that have been addressed in developing the method and, through 2D and 3D validation cases, demonstrates advantages over some established methods.

1 INTRODUCTION

A number of well-established boundary element methods (BEM or panel methods) exist for computing the steady compressible flow past complex configurations based on Green's functions for the Laplace equation after transformation of the Prandtl-Glauert equation. Despite one of the most successful versions of the panel method being originally developed as a particular form of a general unsteady formulation [1,2], very few methods for computing unsteady flow about realistic geometries have followed. Notable exceptions are the time-domain methods USAERO [3] and Eller [4], and the frequency domain versions of VSAERO [5] and PANAIR [6].

By contrast, methods akin to the more approximate planar vortex lattice method (VLM) for unsteady flows have thrived, in particular the doublet lattice method (DLM) [7]. More recently, methods based on solution of the unsteady Euler and RANS equations have received considerable attention, along with methods for the efficient utilisation of these CFD codes. There is a gap in the spectrum of methods between DLM and full CFD.

This paper describes the development, testing and application of an unsteady version of NEWPAN, a steady panel method that has been used extensively in aerospace, marine and automotive applications. The purpose of developing an unsteady version of NEWPAN was to permit rapid solutions of unsteady flow about the actual geometry preserving the ease of use that NEWPAN has provided for steady flows.

2 FORMULATION

2.1 Core solver

The NEWPAN boundary element method for steady, compressible flows is based on the Dirichlet formulation as described by Morino [1] extended to allow for unsteady, compressible flows with solutions being obtained in the frequency domain.

The fundamental approach is to represent the total velocity potential as the sum of a steady and unsteady part and take the velocity potential as the real part of:

$$\Phi(x, y, z, t) = \phi_s(x, y, z) + \exp(-i\omega t)\phi_u(x, y, z)$$

Instead of just one parameter (the Mach number M , the ratio of onset flow speed U to the undisturbed sound speed a) in steady flow, the solutions now depend on a frequency ω through the frequency parameter $k = \dfrac{\omega L}{U}$.

2.2 Compressibility correction

The Göthert Type 2 coordinate transformation has been used to reduce the second-order spatial gradient terms so that they reduce to a Laplacian. A key issue in using this transformation is that the normal to the surface in the untransformed (physical) space does not transform to the normal to the surface in the transformed space. This means that the normal velocity in the physical space comprises contributions from the normal *and* tangential velocities in the transformed space. The relative magnitude of the tangential velocity contribution to the physical space normal velocity depends on the windward component of the normal vector, so this effect is pronounced for blunt-nosed bodies.

2.3 Reduction to Helmholtz equation

A further transformation of the velocity potential is then performed that removes the first-order spatial gradient from the Göthert-transformed equation and reduces the equation to a Helmholtz equation.

The possible combinations of M and k and their interpretation in terms of the type of solutions they correspond to are summarised in the following table where $\phi(x, y, z, t)$ is the real part of $\exp(-i\omega t)\overline{\phi}(x, y, z)$:

M	k	$\overline{k}$	Equation	CASE
0	0	$0\ (= Mk)$	$\dfrac{\partial^2\overline{\phi}}{\partial x^2} + \dfrac{\partial^2\overline{\phi}}{\partial y^2} + \dfrac{\partial^2\overline{\phi}}{\partial z^2} = 0$	Laplace (incompressible, steady and unsteady)
> 0	0	$0\ (= Mk)$	$(1 - M^2)\dfrac{\partial^2\overline{\phi}}{\partial x^2} + \dfrac{\partial^2\overline{\phi}}{\partial y^2} + \dfrac{\partial^2\overline{\phi}}{\partial z^2} = 0$	Prandtl-Glauert (compressible, steady)
0	> 0	$\dfrac{\omega L}{a}$	$\dfrac{\partial^2\overline{\phi}}{\partial x^2} + \dfrac{\partial^2\overline{\phi}}{\partial y^2} + \dfrac{\partial^2\overline{\phi}}{\partial z^2} + \overline{k}^2\overline{\phi} = 0$	Static Helmholtz
> 0	> 0	Mk	$(1 - M^2)\dfrac{\partial^2\overline{\phi}}{\partial x^2} + \dfrac{\partial^2\overline{\phi}}{\partial y^2} + \dfrac{\partial^2\overline{\phi}}{\partial z^2} - 2i\overline{k}M\dfrac{\partial\overline{\phi}}{\partial x} + \overline{k}^2\overline{\phi} = 0$	Translating Helmholtz
> 0	> 0	$\dfrac{Mk}{\sqrt{1 - M^2}}$	$\dfrac{\partial^2\tilde{\phi}}{\partial x^2} + \dfrac{\partial^2\tilde{\phi}}{\partial y^2} + \dfrac{\partial^2\tilde{\phi}}{\partial z^2} + \overline{k}^2\tilde{\phi} = 0$	Transformed translating Helmholtz

2.4 Helmholtz Solver

The final version of the transformed equation is a Helmholtz equation, as also used in acoustics studies. In the majority of boundary element methods for solving the Helmholtz equation the integrals over the surface arising in the BEM formulation are evaluated using Gaussian integration over each panel, sometimes with the use of parametric elements. This leads to difficulties with the hyper-singular form of the integral if a Neumann formulation is used. Here we take advantage of the fact that our discretisation is based on flat panels carrying constant doublicity and source strength to reduce the surface integrals to edge integrals. This has the additional advantage that as the solution procedure is based on the use of collocation points in the panel centre the issue of hyper-singular integrals is avoided.

2.5 Spurious modes

Many acoustics studies using the boundary element method for solving the Helmholtz equation highlight the issue of 'spurious modes', where internal eigensolutions for thick bodies contaminate the outer solution. In the context of a Dirichlet method this manifests itself as internal solutions that have zero potential on the inside of the surface, but non-zero normal velocity at the surface and vice-versa for Neumann formulations.

Two main methods are available for circumventing this problem. The first is the CHIEF [8,9] method where additional collocation point are placed inside the body and the Dirichlet condition of zero perturbation potential at those points is also enforced. This leads to an over-determined equation set that is usually solved in a least-squares sense. A disadvantage of this approach is that no guidance is available on the placing of the internal points in the general case, and if they lie at nodal points of the solution then the method fails.

The other approach is due to Burton and Miller [10]. They prove that a linear combination of the Dirichlet and Neumann formulation, where the two solutions are added via a complex weighting term, will avoid the spurious solutions occurring. In simplistic terms as both the Dirichlet (potential) and Neumann (velocity) boundary conditions are being applied both these have to be correct value and so spurious solutions are nullified. This, of course, requires the construction of the influence matrix for both the Dirichlet and Neumann problems but results in the same size of square matrix as the Dirichlet problem.

The present method uses the Burton-Miller approach, as the underlying BEM method uses Dirichlet and Neumann formulations interchangeably[1] so the required influence functions are already available. Furthermore, the Burton-Miller approach is 'carefree' is the sense that it does not depend on the arbitrary selection of extra internal collocation points or knowledge of where spurious solutions may occur.

2.6 Unsteady form of the Bernoulli equation

The general form of the Bernoulli equation for potential flow, referred to still-air axes, is:

$$\frac{1}{2}\nabla\Phi.\nabla\Phi + \frac{\partial\Phi}{\partial t} + \int \frac{dp}{\rho} = H(t) \tag{1}$$

[1]The Dirichlet formulation cannot be used for bodies of zero thickness, like a vortex lattice, hence we use a hybrid method that permits the use of both thick and thin components in a configuration

where Φ is the total velocity potential (both steady and unsteady components) and $H(t)$ is the total enthalpy that can vary with time but not in space. As this is expressed in an axes system fixed in still air, and all fluid motions (and thus Φ) are assumed to decay to zero far from the body, the value of $H(t)$ is the constant H_o.

We may regard the total enthalpy as comprising a kinematic term:

$$\frac{1}{2}\nabla\Phi.\nabla\Phi + \frac{\partial\Phi}{\partial t}$$

and a 'thermodynamic' term:

$$\int \frac{dp}{\rho}$$

It is only the kinematic terms that concern us here. As we are concerned with the solution on the (translating/deforming) surface it is convenient to work exclusively with surface values of the velocity potential and the above Bernoulli equation has to be modified to account for the motion of the surface. The most concise description of this effect is that the (inertial) time derivative with inertial coordinates (X, Y, Z) fixed is related to the time derivative with intrinsic body coordinates $(\xi\eta, \zeta)$ fixed via:

$$\left.\frac{\partial}{\partial t}\right|_{X,Y,Z} = \left.\frac{\partial}{\partial t}\right|_{\xi,\eta,\zeta} - \vec{U}.\nabla\Phi$$

Where $\vec{U}$ is the inertial velocity of the point on the surface. As an example of the consequences of this effect, we consider the kinematic part of the Bernoulli equation for thin components, using the decomposition of the potential into the steady and unsteady parts shown above. The result for the kinematic part of the unsteady pressure jump across a thin surface is then found to be:

$$(-\vec{U}_s + \overline{\nabla\phi_s}).\nabla(\Delta\phi_u) + (-\vec{U}_u + \overline{\nabla\phi_u}).\nabla(\Delta\phi_s)$$

where $\vec{U}_s$ is the steady part of the body motion through the inertial space and $\vec{U}_u$ is the unsteady part. The overbars denote the mean part and the Δ are the jump terms (The gradients implied by ∇ are therefore just taken in the surface). Note this is a product involving the *total* mean tangential velocity (body motion plus perturbation) and the jump in perturbation velocity across the surface.

The first term is the conventional term used in DLM, apart from the inclusion of the steady velocity perturbation. We have an additional second term where $\vec{U}_u$ is parallel to the surface for in-plane motions as is the term $\overline{\nabla\phi_u}$. These are taken as a scalar product with $\nabla(\Delta\phi_s)$. In DLM there is no steady loading, so $\nabla(\Delta\phi_s)$ is zero and this product vanishes. However, for the general case these terms must be included in the pressure calculation across a thin surface. This is a term that is important in the T-tail problem and is included naturally in the present formulation.

An important consequence of this treatment of the Bernoulli equation is that the conventional aerodynamic influence coefficients (AICs) [11] relating pressures on the surface to the aerodynamic downwash are not sufficient to define the loading on the surface. The case of in-plane motions discussed above has no unsteady downwash but there is an unsteady load induced, which the conventional AIC approach would neglect.

3 VALIDATION

Because of the special issues that arise with an unsteady compressible BEM, a large number of test cases have been used in the development of USNEWPAN. Each tests a particular aspect of the method as described below.

3.1 Testing of Helmholtz solver

Initial testing of the core Helmholtz solver was carried out against analytic solutions (acoustic scattering of a sphere, the flow induced by translating and oscillating sources inside a translating sphere). Fig. 1 shows the analytic and computed results using the Dirichlet-only form of the Helmholtz solver (i.e. the Burton-Miller method is not implemented) for the scattering potential on the surface of a sphere subject to an incident acoustic wave is shown. The frequency of the incident wave corresponds to the second eigenmode for interior waves in a sphere. The real part of the solution is grossly in error and the error does not decrease with increasing the number of panels. Furthermore this erroneous solution does not exhibit any feature that would indicate it is in error if the exact solution was not known. The eigenfrequencies for a sphere are well-known so the issue of spurious solutions can be anticipated and have been used to generate this test case. Such eigenfrequencies are not easily available for general bodies so there is a danger that incorrect solutions could be obtained unknowingly. Fig. 2 shows results for the same case where the Burton-Miller hybrid scheme is used and clearly shows the effectiveness of this approach.

3.2 Thick body tests

To test the calculation of pressures allowing for the motion of the body, analytic results for the incompressible flow past an ellipsoid in arbitrary motion were derived. This rests on the classical solution for the flow past ellipsoids described by Lamb [12]. As the flow is incompressible and the body is non-lifting there are no history ('circulatory') effects in the solution which is determined by the instantaneous motion of the body. From this an analytic linearized solution of the flow past an ellipsoid at arbitrary incidence undergoing small oscillations in pitch and heave was obtained[2]. In fact this extends work described by Jones [14] in the 1920's while investigating the pressures on airship hulls in turning flight.

Fig. 3 shows the real and imaginary (in/out phase) components of the pressure coefficient on the windward generator of a pitching ellipsoid of axis ratio 4 in incompressible flow as computed by USNEWPAN compared with the analytic solution. The agreement is excellent showing that the treatment of the additional term in the Bernoulli equation due to body motion has been correctly implemented.

[2]Geißler [13] obtained solutions for the same problem via a numerical approach and his results have been used elsewhere to validate other methods.

3.3 Thin Wing Validation

Given the support for thin (double sided) panels, it is possible to validate the unsteady aerodynamic solver directly against solutions for a flat plate. Modes examined include heave, pitch, an oscillating flap, and response to gusts.

If a subset of USNEWPAN capability is used, namely thin only and with no mean/steady loading, then comparison may be made with the well established and popular Doublet-Lattice Method [7]. In this case, direct comparisons with DLM were made for the three-dimensional loading on a low aspect ratio wing, and also the two dimensional pressures and loadings at the centreline for a high aspect ratio wing.

Figures 4 to 7 show the convergence behaviour for NEWPAN in comparison to DLM. The case presented is an aspect ratio one rectangular wing, oscillating in pitch about its mid-chord at a reduced frequency (based on semichord) of 2.0 and a Mach number of 0.8. This follows the work of Rodden et al [15], who have studied DLM behaviours previously. An implementation of DLM in use at DLR [16] was used in this comparison, which includes the quartic approximation to the numerator of the downwash factor in the oscillatory kernel function.

Models of the rectangular wing were prepared with differing box/panel densities, ranging from 10 to 120. In all cases the full span wings had the same relative number of chordwise and spanwise boxes (panels), but left/right symmetry was exploited to reduce problem size. Hence the panel counts for DLM and NEWPAN are equal; DLM uses an equidistant spacing hence maintains a box aspect ratio of 1.0, whereas NEWPAN uses a full-cosine distribution over the chord and half-cosine across the semispan. Such a distribution is desirable for NEWPAN but undesirable for DLM due to the high panel aspect ratios near the leading and trailing edges.

Figures 4 and 5 show the the real and imaginary parts of wing lift coefficient, plotted against $1/N$ where N is the chordwise (and spanwise) panel density. Similarly, figures 6 and 7 show the percentage error from the fully converged Re/Im lift coefficients, versus N. Rates of convergence are higher, and percentage errors lower, when comparing NEWPAN to DLM.

Figures 8 and 9 show the effect on the loading at the centreline as the wing is increased in aspect ratio, with plots of the real and imaginary parts of the centreline sectional wing lift coefficients, respectively. The wing is oscillating in heave, at a reduced frequency (based on semichord) of 2.0 and a Mach number of 0.8. As the aspect ratio increases, the solution converges towards the analytic 2D solution due to Possio, although convergence of the real part of the DLM result is less satisfactory. 40 chordwise by 20 spanwise (i.e. 800 total) panels were used in each NEWPAN model, and 40 chordwise by 40 spanwise (i.e. 1600 total) panels in the case of DLM. Despite double the panel count wrt NEWPAN, DLM has greater difficulty in cases with combinations of high reduced frequency and aspect ratio; this is examined in more detail below. Results show that the choice of an aspect ratio of 20 should provide behaviour at the centreline very close to a two-dimensional result.

Two-dimensional analytic solutions, such as those due to Theodorsen and Possio [17–19], may be used in this comparison by considering the results on the centreline of a very high aspect ratio rectangular wing. Figures 11 to 15 show results for the sectional pressure

distribution ΔC_p at the centreline of a thin wing of aspect ratio 20, at zero degrees mean incidence, undergoing oscillatory motions or subject to an onset gust profile. NEWPAN results are compared to those generated by DLM, and also to the 2D results from a code solving Possio's integral equation [20]. These cases are for a Mach number of 0.6 and a reduced frequency (based on semichord) of 1.0.

Efforts were made to ensure that the chordwise and spanwise panel densities met or exceeded the guideline minimums established by Rodden and others [15, 21] for DLM (with a quartic kernel approximation). For example, 20 boxes chordwise give 63 boxes per wavelength, and 40 boxes (semi-)spanwise give a box aspect ratio of 5. This gives a total number of boxes of 800. The NEWPAN equivalent models also used 800 panels. NEWPAN does not suffer from panel aspect ratio constraints to anything like the same degree as DLM, and optimum results on a thin wing are generally obtained by using a full-cosine distribution (bunched at leading and trailing edges) in the chordwise direction, with a half-cosine distribution (bunched at the tip) in the spanwise direction. This gives a maximum panel aspect ratio for this model of 510; NEWPAN models with panel aspect ratios in the several thousands present no difficulties.

It is useful, due to the presence of the leading edge singularity, to plot a transformed form of the pressure distribution i.e. $\sqrt{\frac{x - x_{LE}}{c}}\Delta C_p$ rather than raw ΔC_p. This produces plots with finite ranges where the differences between results are more readily apparent.

Figure 10 shows results for an oscillatory flap mode, with a hingeline at x/c = 0.8. NEWPAN results follow the Possio results very closely. For the flap mode only, Possio results suffer from a degree of waviness. DLM results are less good.

In an effort to improve the DLM results, the DLM model was refined further, to 40 boxes chordwise and 60 boxes spanwise and hence 2400 boxes total. These values translate into 126 boxes per wavelength, and a box aspect ratio of 6.66. The corresponding DLM results are shown in figure 11; USNEWPAN results are superior to refined DLM results, using a third of the number of panels.

USNEWPAN execution time for this case on a modern desktop PC, taking advantage of the multi-core CPU, was 12 seconds for results for the flap mode, or 13 seconds for a full AIC. DLM execution time to compute the AIC was 40 seconds at the higher density, and 5 seconds at the lower density. Possio run time was 12 seconds. All run times are indicative only.

For the remaining modes, the denser 2400 box models were used for the DLM, with 800 panels for the NEWPAN models.

Figure 12 shows results for centreline pressures for the wing undergoing a heaving motion, while figure 13 shows the corresponding results for the response to a sinusoidal vertical gust, also of frequency $k = 1$ (based on semichord).

The results for centreline pressures for the wing undergoing a pitching oscillation about midchord are given in figure 14, again at $k = 1.0$.

Figure 15 also shows results for pitch, but at a higher frequency of k=4. This case demonstrates the constraints that DLM suffers from when modelling high aspect ratio wings at

high reduced frequency. The wavelength is now $\pi/4$, hence DLM requires a minimum 64 chordwise panels to achieve 50 boxes per wavelength. Likewise 64 boxes will be required across the semispan to achieve a maximum box aspect ratio of 10. Hence the DLM model has been run with 4096 boxes, in contrast to the NEWPAN model which still has 800 panels; the smaller (and faster) NEWPAN model returns notably better results.

3.4 The Effect of Thickness and Mean Incidence

The formulation of the method allows direct comparison of thin and thick wing results within the same solver. For thick wings, USNEWPAN returns surface pressures, i.e. C_p per panel/vertex. For thin wings, USNEWPAN can return distinct C_p values for both the top and bottom of the panel/vertex, in addition to the ΔC_p jump. Chordwise integration of the sectional centreline pressures gives the sectional lift coefficients presented here.

Figure 16 shows the effect of wing thickness on the lift coefficient of a high AR wing pitching about its midchord. Each line shows the variation in Real vs. Imaginary C_l as the reduced frequency increases (in the clockwise direction) in the range 0.1 to 4.0, at a Mach number of 0.6. The zero thickness flat plate result is compared to those from wings of a NACA 4-series basic thickness form, scaled to 6% and 12% thickness to chord ratio. The magnitude and effect of thickness across the range of reduced frequencies is demonstrated.

Figure 16 also shows the effect of increasing the mean, steady incidence. Steady loading affects the unsteady perturbation significantly, as shown by the effect of a 15 degree incidence applied to the thin wing.

3.5 LANN wing

The LANN wing is Dataset 9 from the AGARD compendium of unsteady aerodynamic measurements [22, 23]. This is an isolated wing of aspect ratio 8, with a leading edge sweep of 28 degrees, with a 12% thick supercritical aerofoil profile. It was tested in a wind tunnel in steady flow and in additional tests with the wing undergoing a pitch oscillation about a spanwise axis running through the 62.1% root chord location. Experimental data is available in the Mach range 0.6 to 0.95.

Results from run number 22 are presented here, with a mean incidence of 0.6 degrees, Mach number 0.621 and a reduced frequency based on (full) root chord of 0.266.

Comparisons with results from the Euler code EUVISC [24] are also shown.

Fig. 17 shows the wing planform, with three spanwise stations shown at 20%, 47.5% and 82.5% semispan. Steady and unsteady results are presented for each of these three spanwise stations in turn in Figures 18, 19 and 20. In the first plot at each station, steady pressures from NEWPAN and EUVISC are compared with experiment. Also shown are the $M = 0$ incompressible NEWPAN results, to demonstrate the effects of compressibility. Results are excellent over the majority of the chord; errors at the suction peak are due to near sonic local Mach number and at the trailing edge are due to local modification of the profile for EUVISC and NEWPAN results to provide a thin trailing edge. The other two plots at each spanwise station show the real and imaginary parts of the unsteady pressures per unit pitch amplitude. Experimental results for the imaginary part (especially near the tip) are seen to be too noisy to make firm comparisons with experiment.

4 NEWPAN IMPLEMENTATION

NEWPAN/USNEWPAN provides a modern implementation of a boundary element method, written in C++ with object-oriented design, dynamic memory allocation, and shared memory multi-threading using OpenMP.

Given the dependence of unsteady loads on the mean flow, the first stage of an analysis is the computation of the steady solution (e.g. about the trimmed configuration with static aeroelastic deformation). The oscillatory unsteady solution proceeds as a perturbation to the full steady solution. The modelling flexibility of mixed thin and thick, structured and unstructured patches is available throughout. The unsteady solution may be for specified mode(s), or a complete AIC generated. Modal calculations can be requested for an arbitrary input vector of vertex deflections. Rigid body modes are supported directly. Control surfaces are defined via their geometry (hinge line and surface extents) in a panel independent fashion, allowing control modes to be generated. Multiple Mach numbers and reduced frequencies can be requested during a single run.

The AIC matrices are stored to an HDF5 dataset (Hierarchical Data Format). This provides a powerful and convenient method of storing platform neutral binary data, with API's freely available for all common scientific programming languages such as C++, FORTRAN, Python and MATLAB.

The AIC dataset provides all the matrices required to generate vertex-based force output directly from any set of modal vertex-based deformations. Gust velocities and velocities due to manoeuvre are also supported as input, and both panel-based and vertex-based Cp's can be output. In general the AIC matrices are complex, but solutions at a reduced frequency of zero are also supported and lead to real-only matrices for use in quasi-steady and static aeroelastic cases. The core AIC matrices are fully populated (number of panels squared) and are specific to M,k and steady trim. However some of the stencil matrices (e.g. velocity potential to pressure coefficient) are sparse and are stored efficiently using COO format. Furthermore, the contributions due to surface motion can be stored in a frequency independent fashion, giving significant savings in storage requirements for AIC's covering a large range of reduced frequencies.

Previous work with USNEWPAN has also included support for the direct export of a NASTRAN external aerodynamic database for use with a NASTRAN (SOL=145) input for flutter calculations. Export to the NASTRAN database is performed via calls to the NastAero library, implemented via the MSC.Nastran toolkit [11].

A NASTRAN coupled calculation has been performed on a complete Freedom 4 (FR-4) general aviation aircraft configuration. A trim calculation was performed for a cruise condition, and AIC's exported to the NASTRAN database. The USNEWPAN derived aerodynamic AIC's were then used to perform a flutter calculation.

Figure 21 shows the FR-4 configuration, complete with instantaneous pressures at sections through port and starboard tailplane due to a fuselage torsional mode, at different times during the oscillatory cycle. Visualisation within the VIEWPAN post-processor enables animation through the cycle, and the display of sectional pressure distributions as 2D plots referenced within the 3D view.

5 CONCLUSION

A new boundary element method for unsteady, subsonic compressible flow past realistic geometries has been described. Fundamental issues of the possibility of spurious solutions, careful treatment of the Bernoulli equation for moving surfaces and the avoidance of the problem of hyper-singular integrals have been addressed. Comparison of the method with results from analytic test cases show excellent agreement and comparisons with earlier numerical methods show marked improvement in convergence behaviour.

The inadequacy of conventional AIC matrices solely relating pressures to the normal wash has been discussed. The present formulation captures the terms associated with body motion and steady loading. The implementation described enables generation of vertex based forces directly from vertex based deformations, or velocities due to gusts or manoeuvre.

REFERENCES

[1] L. Morino and C. Kuo. Subsonic potential aerodynamics for complex configurations: A general theory. *AIAA Journal*, 12(2):191, 1974.

[2] L. Morino and K. Tseng. Steady, oscillatory and unsteady, subsonic and supersonic aerodynamics (soussa) for complex aircraft configurations. *AGARD-CP-227, AGARD Symposium on Unsteady Aerodynamics, Ottawa, Canada*, 1977.

[3] B. Maskew. A timestepping analysis method for the flow about multiple bodies in general motions, user manual. *Technical Report, Analytical Methods, Inc., Redmond, WA*, 1990.

[4] David Eller and Martin Carlsson. An efficient aerodynamic boundary element method for aeroelastic simulations and its experimental validation. *Aerospace Science and Technology*, 7:532–539, 2003.

[5] James K. Nathman. Potential-based panel method for oscillatory motion. *AIAA Paper 2006-1255, 46th AIAA Aerospace Sceinces Meeting*, 2006.

[6] Arthur R. Dusto and Michael A. Epton. An advanced panel method for analysis of arbitrary configurations in unsteady subsonic flow. *NASA CR-152323*, 1980.

[7] E. Albano and W.P. Rodden. A doublet lattice method for calculating lift distributions on oscillating surfaces in subsonic flow. *AIAA Journal*, 7(2):279–285, 1969.

[8] H.A. Schenk. Improved integral formulation for acoustic radiation problems. *J. Acoust. Soc. Am.*, 44(1):41–58, 1968.

[9] L.G. Copley. Fundamental results concerning integral representations in acoustic radiation. *J. Acoust. Soc. Am.*, 44(1):28–32, 1968.

[10] A.J. Burton and G.F. Miller. The application of integral equation methods to the numerical solution of some exterior boundary value problems. *Proc. Roy. Soc. London Ser. A*, 323:201–210, 1971.

[11] Johannes Wandinger. NastAero - a generic interface to external aerodynamics, programmer's manual. *MSC Report*, 1982.

[12] H. Lamb. *Hydrodynamics*. Cambridge University Press, 6th edition, 1974.

[13] Wolgang Geißler. Der harmonisch schwingende rumpf in unterschallströmung: Einfluß der kompressibilität. *DFVLR Forschungsbericht DFVLR-FB 78-24*, 1978.

[14] R. Jones. The distribution of normal pressures on a prolate ellipsoid. *Phil. Trans Roy. Soc. Lond.*, 226:231–266, 1927.

[15] W.P Rodden, P.F. Taylor, and S.C. McIntosh. Improvements to the doublet-lattice method in MSC/NASTRAN. *Paper 3799, MSC.Software Aerospace Users' Conference*, 1999.

[16] T. Kier and M. Leitner. DLR Institute of System Dynamics and Control.

[17] Th. Theodorsen. General theory of aerodynamic instability and the mechanism of flutter. *NACA Report 496*, 1934.

[18] C. Possio. L'azione aerodinamica sul profilo osicllante in un fluido compressibl a vlecoita iposonora. *Aerotecnica*, XVIII(4):441–458, 1938.

[19] H.G. Küssner and L. Schwarz. The oscillating wing with aerodynamically balanced elevator. *NACA Tech. Memo. 991*, 1941.

[20] V. Carstens. Berechnung der instationaeren druck-verteilung an harmonisch schwingenden gittern in ebener unterschallstroemung. *DFVLR IB 253-75J02 DFVLR-AVA, Goettingen*, 1975.

[21] L.H. van Zyl. Robustness of the subsonic doublet lattice method. *Aeronautical Journal*, 107 (1071):257–262, 2003.

[22] AGARD. Compendium of unsteady aerodynamic measurements. *AGARD Report No.702*, 1982.

[23] AGARD. Compendium of unsteady aerodynamic measurements. *AGARD Report No.702, Addendum 1*, 1985.

[24] H.H. Henke. The viscous-coupled 3D Euler method EUVISC and its aeroelastic application. *International Forum for Aeroelasticity and Structural Dynamics*, II:95–106, 2001.

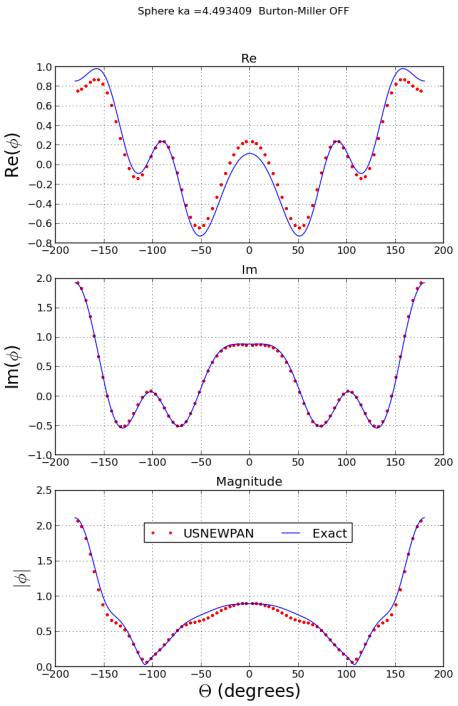

Figure 1: Acoustic scattering: Dirichlet only

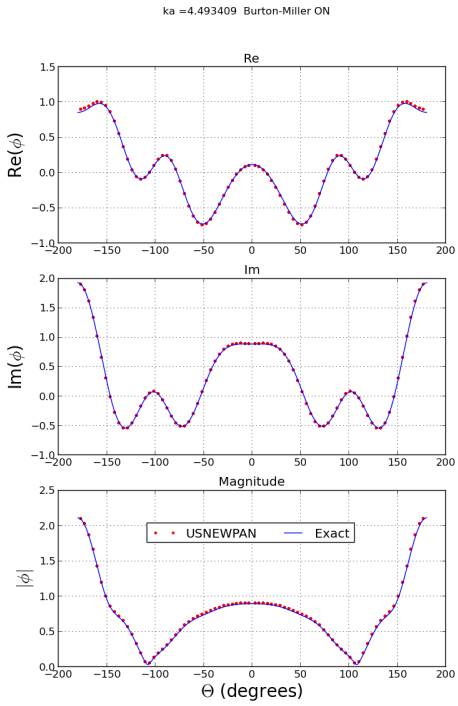

Figure 2: Acoustic scattering: Burton-Miller

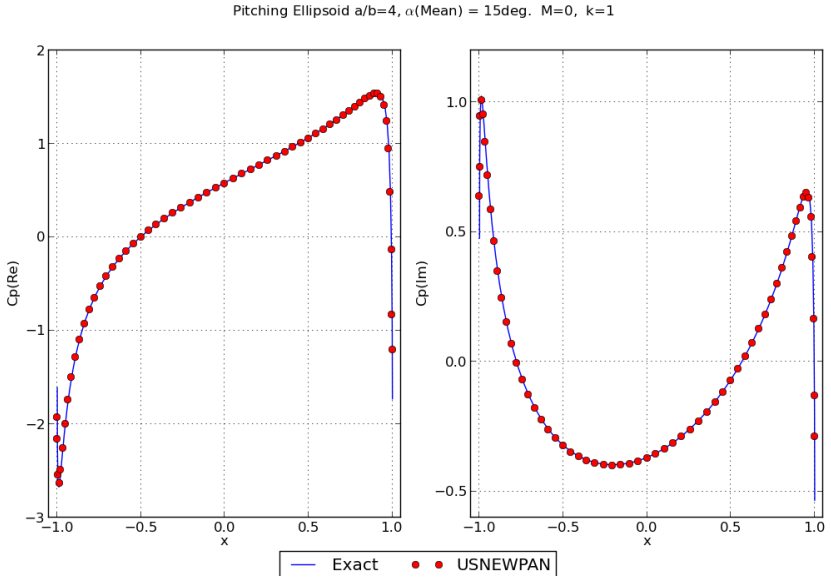

Figure 3: Pitching ellipsoid; $a/b = 4$

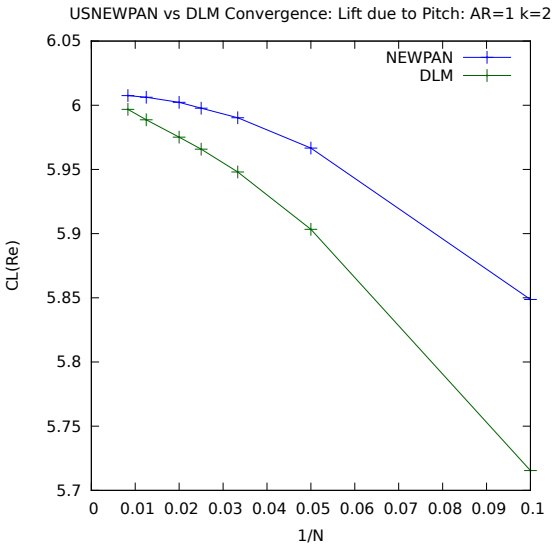

Figure 4: $AR = 1$ Wing : Convergence

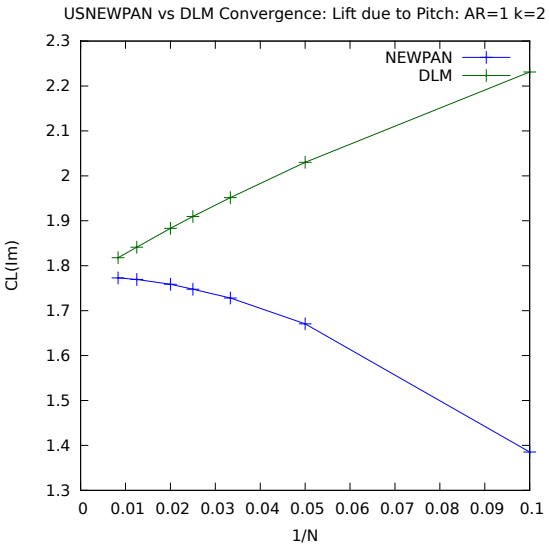

Figure 5: $AR = 1$ Wing : Convergence

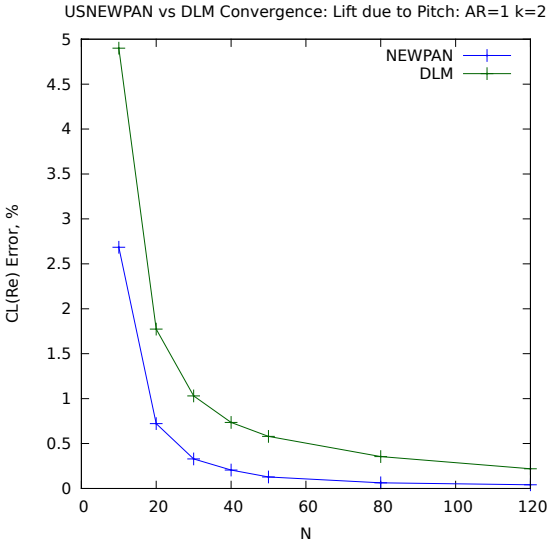

Figure 6: Real Part of C_L : Error level

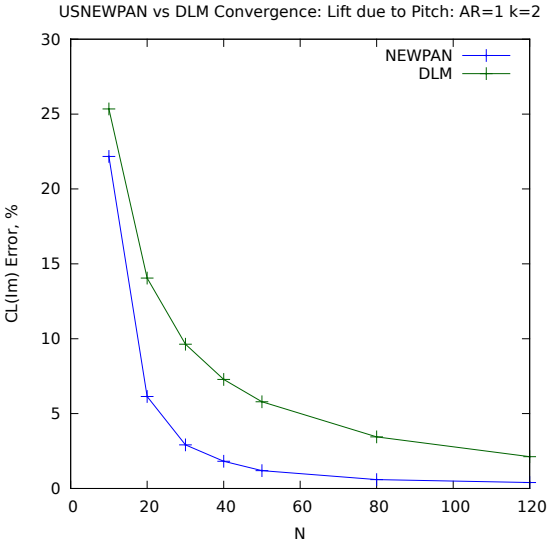

Figure 7: Imaginary Part of C_L : Error level

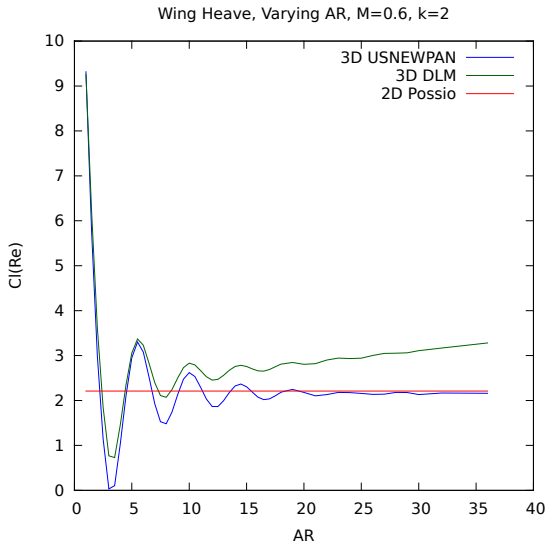

Figure 8: Wing Heave: Varying AR

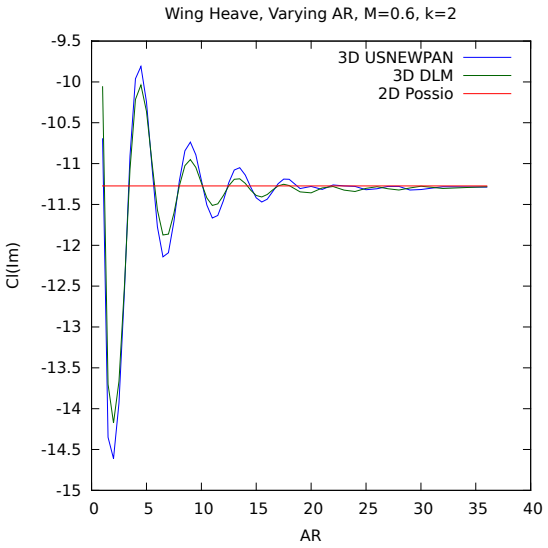

Figure 9: Wing Heave: Varying AR

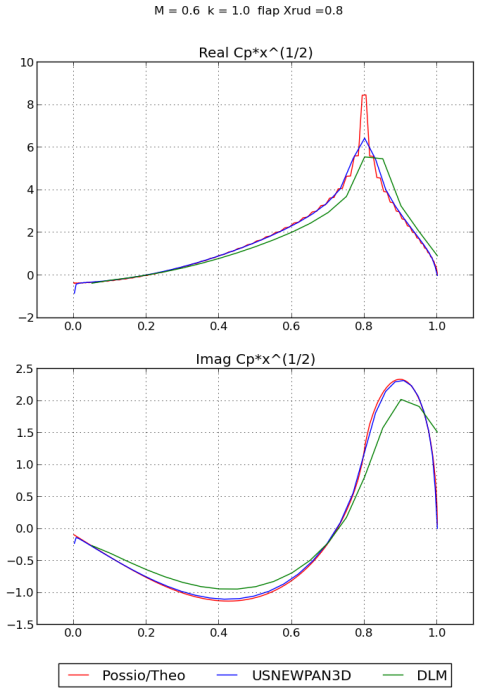

Figure 10: Flap Mode: Centreline C_p

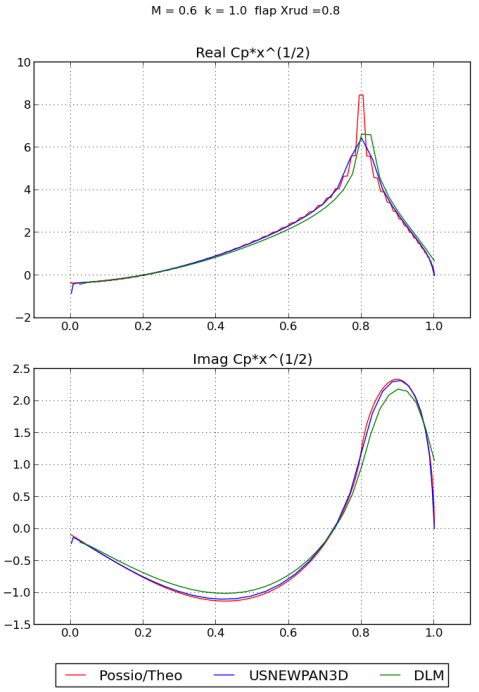

Figure 11: Flap Mode: 2400 DLM boxes

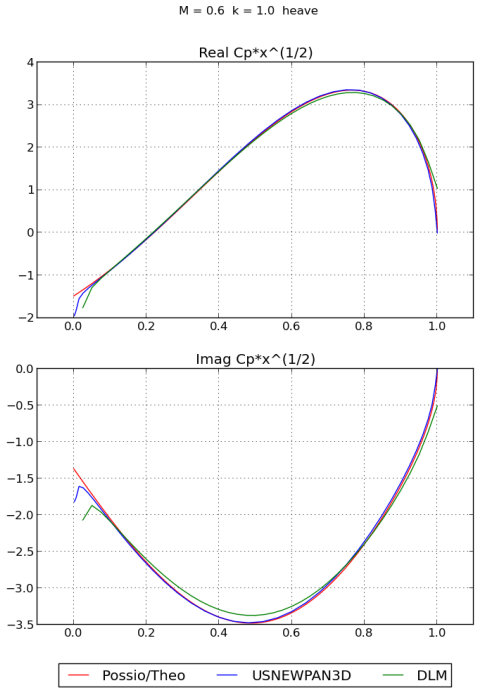

Figure 12: Heave Mode: Centreline C_p

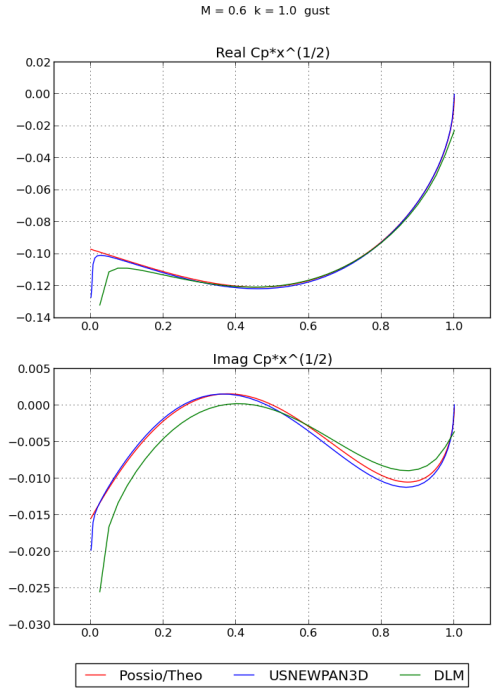

Figure 13: Centreline C_p due to vertical gust

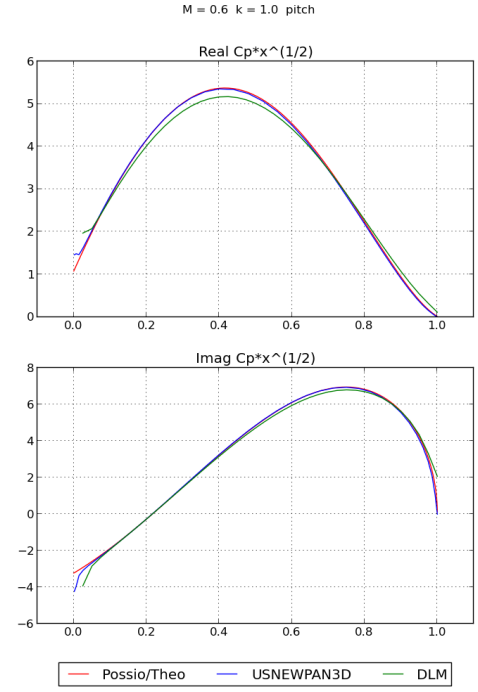

Figure 14: Pitch Mode, $k = 1$: Centreline C_p

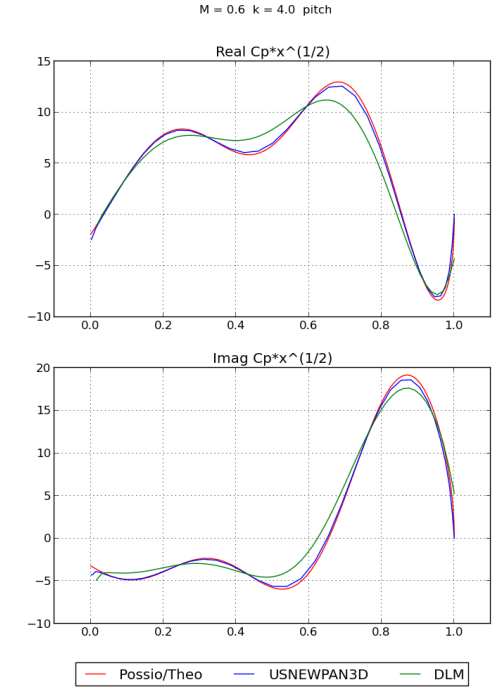

Figure 15: Pitch Mode, $k = 4$: Centreline C_p

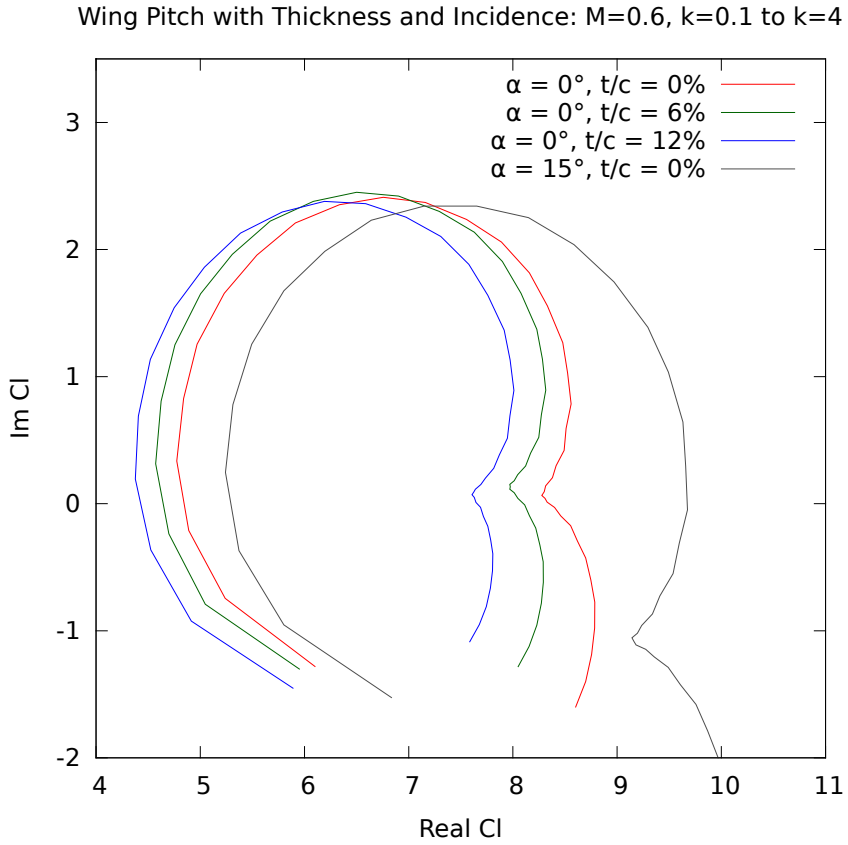

Figure 16: Wing Pitch Frequency Response: Effect of Thickness and Mean Incidence

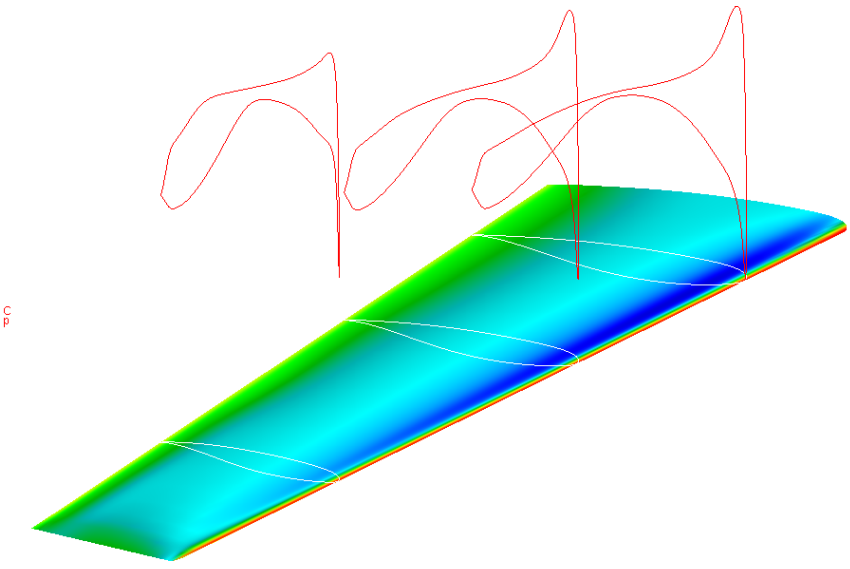

Figure 17: LANN Wing: Sections at $\eta = 0.2, 0.475, 0.825$

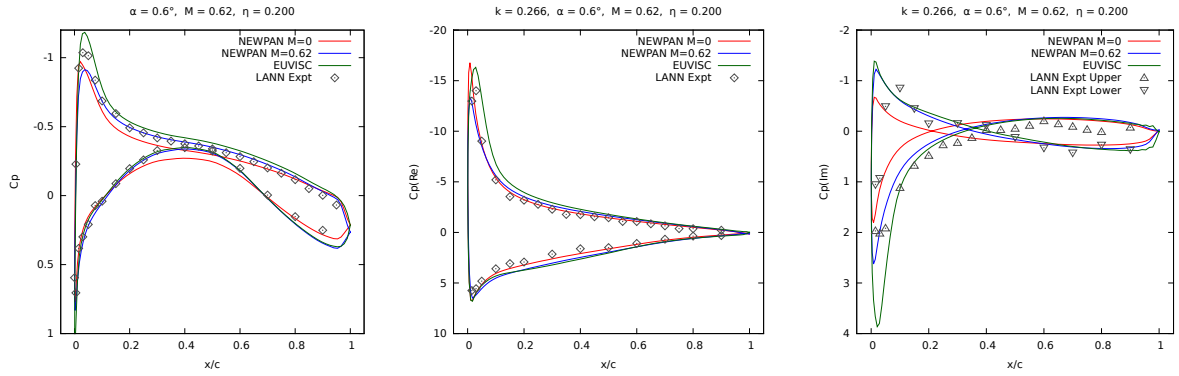

Figure 18: LANN Wing $\eta = 0.200$

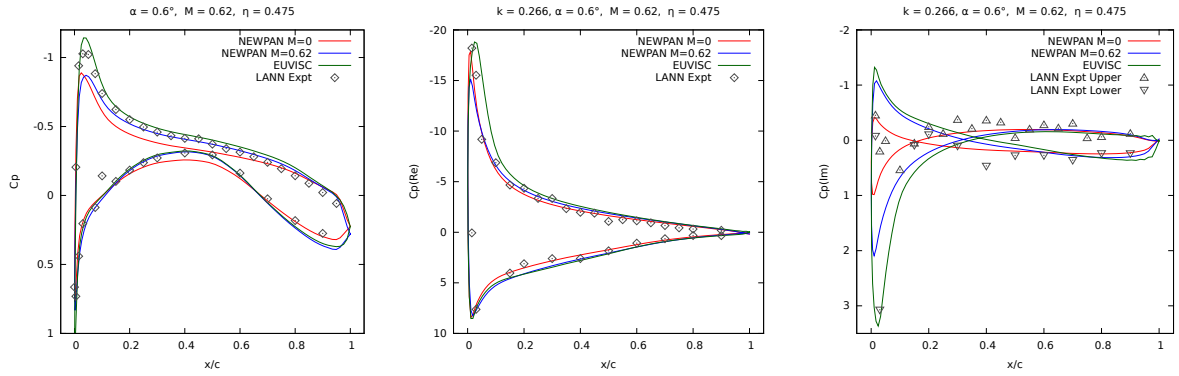

Figure 19: LANN Wing $\eta = 0.475$

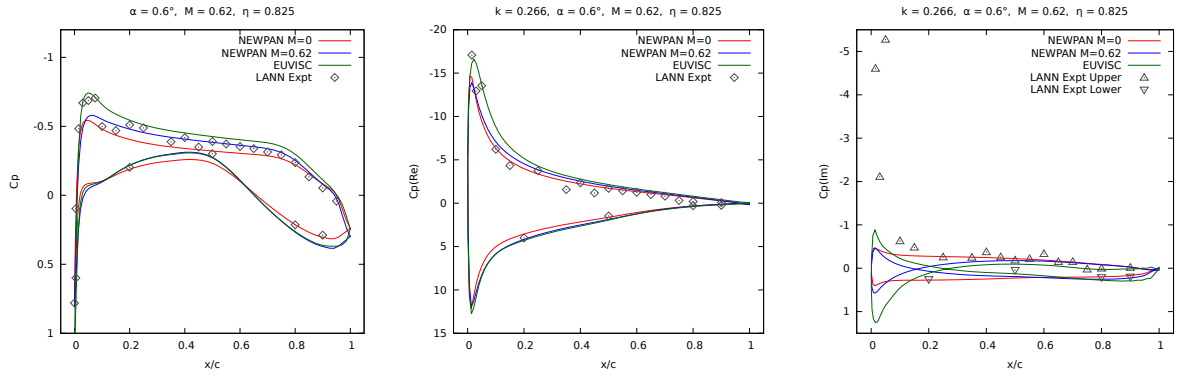

Figure 20: LANN Wing $\eta = 0.825$

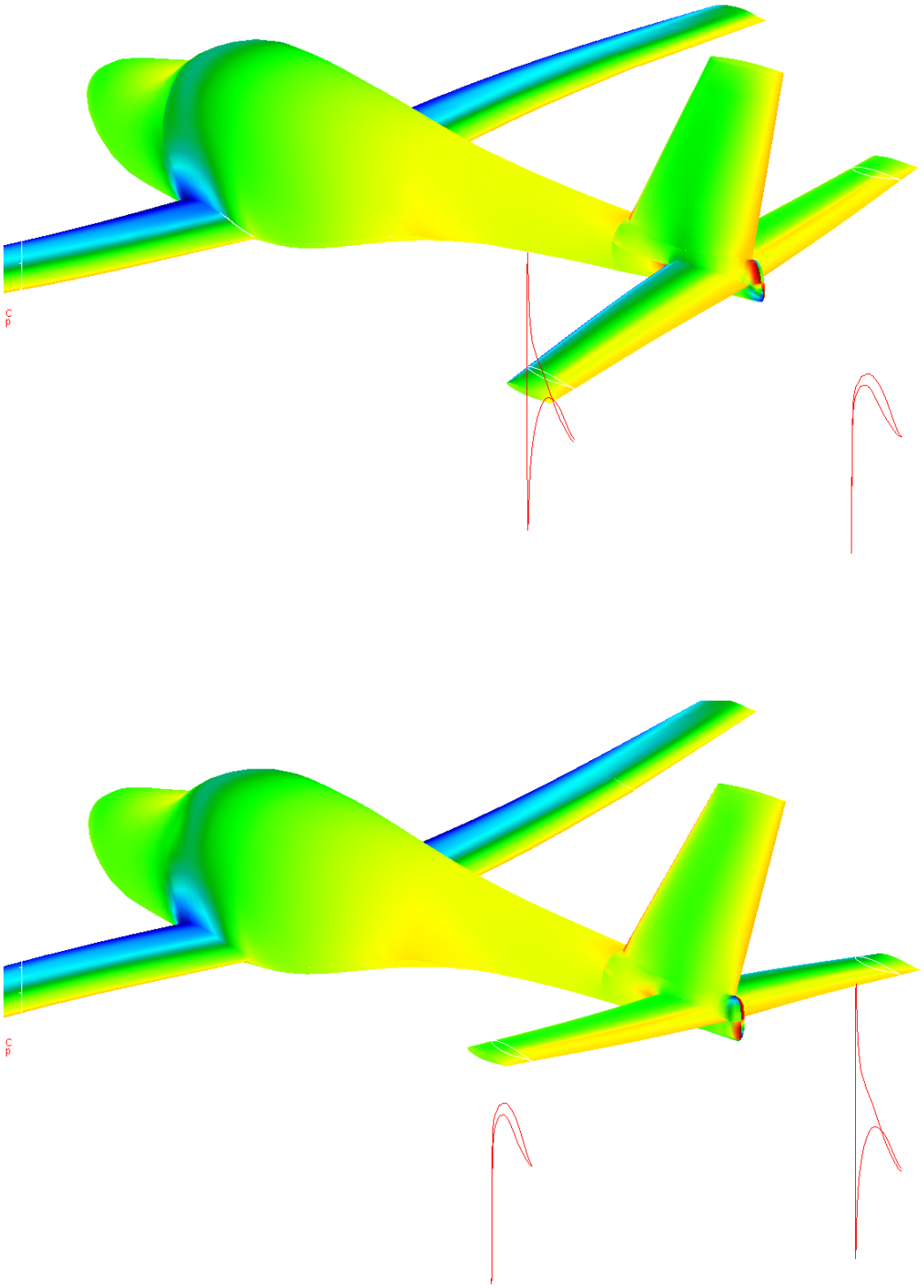

Figure 21: FR-4 GA Aircraft Flutter